IEEE Access
Multidisciplinary ⋮ Rapid Review ⋮ Open Access Journal

Received January 6, 2020, accepted January 20, 2020, date of publication January 29, 2020, date of current version February 6, 2020.

Digital Object Identifier 10.1109/ACCESS.2020.2970271

Inductive Frequency Selective Surface: An Application for Dichroic Sub-Reflectors

JUAN A. VÁSQUEZ-PERALVO[1], JOSÉ-MANUEL FERNÁNDEZ-GONZÁLEZ[1], (Senior Member, IEEE), PAVEL VALTR[2], AND JONATHAN M. RIGELSFORD[3], (Senior Member, IEEE)

[1]Radiation Group, Department of Signals, Systems and Radio Communications, Universidad Politécnica de Madrid, 28040 Madrid, Spain
[2]Department of Electromagnetic Field, Faculty of Electrical Engineering, Czech Technical University in Prague, 166 27 Prague, Czech Republic
[3]Sensata Technologies, Royal Wootton Bassett SN4 8SY, U.K.

Corresponding author: Juan A. Vásquez-Peralvo (jvasquez@gr.ssr.upm.es)

This work was supported by the Spanish Government, Ministry of Economy, National Program of Research, Development and Innovation of the project FUTURE-RADIO "Radio systems and technologies for high capacity terrestrial and satellite communications in an hyperconnected world" under Project TEC2017-85529-C3-1-R.

ABSTRACT An Inductive Frequency Selective Surface (IFSS) self-standing dichroic sub-reflector is presented, which allows the transmission of two frequency bands and reflection of a third band. The operating frequency of the sub-reflector is designed to work at Ku, K and Ka frequency bands, intended for earth to space and space to earth satellite communications. The proposed unit cell is a Jerusalem cross intertwined with an Brigid's cross. The IFSS is investigated using transmission line theory, along with equivalent-circuit model technique. It has been designed, and simulated using CST Microwave Studio and Advance Design Simulator (ADS). The cascade configuration of the IFSS is also investigated to improve frequency roll-off and bandwidth of the reflection and transmission coefficients. The IFSS has been manufactured using two-sided Photo Chemical Machining (PCM) technique, and has been experimentally characterized using an optical configuration, comprising two double ridged horn antennas connected to a VNA and a rotation system. Measured results are in good agreement with theoretical and simulation data, which validates the reliability of the design and manufacturing process.

INDEX TERMS Reflector antennas, equivalent circuits, frequency selective surfaces.

I. INTRODUCTION

Inductive Frequency Selective Surfaces (IFSSs) are electromagnetic filters capable of working as high-pass filters or band-pass filters depending on the resonant element etched in a conductive surface [1]. The main advantage of this type of FSS is the self-standing capability, that is, it can be implemented without a dielectric substrate. Therefore, it will not have frequency shifts due to change of mediums. Additionally, if the conducting surface is thick enough, and manufactured with high hardness metal sheet, it will have mechanical stability [2]. The drawback of dispensing with the substrate are: reduced angular stability, reduced mechanical stability, and increased manufacturing complexity compared with a conventional FSS.

Two methods have been proposed to analyze FSS reflection and transmission coefficients. The first is equivalent circuit method, which was proposed in [3]–[7]. It uses a quasi-static approximation, that is, it considers a uniform distribution of the E- and H-Fields at each point of the surface. This method takes less computational resources than others, and gives a good approximation to real results, even though the FSS is embedded in a stratified medium [4]. The drawbacks of this method are its accuracy, it cannot describe the operation of the FSS at the grating lobe region, and it cannot be used in certain structures like meandered dipole, quadrifilar spiral, and genetically optimized shapes [7]. The second are computational methods, which are the most accurate, and complex methods of both. These offer good approximation at different scenarios, for example, in the case of an FSS with multiple resonant shapes embedded within dielectric loading, the case of an FSS illuminated at different incident angles, and the case of a multi-layer FSS configuration, just to mention a few. Some of those computational methods are: periodic method of moments (PMM) and finite difference

The associate editor coordinating the review of this manuscript and approving it for publication was Gerardo Di Martino.

time domain method (FDTD), which are the most used for these matters [8].

Reducing the weight on a spacecraft, and reducing the area in a satellite is critical, and involves many engineer fields [2]. The satellite dish antenna design challenges comprise an effective reflector design, an optimum multifrequency feed system, and frequency feed segregation. Each of those will be addressed in the following paragraph. First, an effective reflector design can be done using a Cassegrain reflector system with an FSS as dichroic sub-reflector. Second, the FSS allows, for example, using X band and Ku or K frequency bands with the same antenna structure giving multifrequency operation. Finally, the feeds will be isolated due to the dichroic capability. Fig. 1 shows a ray analysis highlighting the antenna design challenges in a satellite.

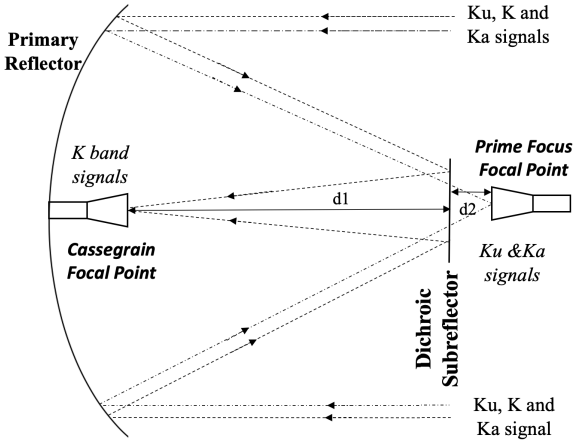

FIGURE 1. Ray analysis of a prime focus Cassegrain reflector using dichroic sub-reflector. The dichroic surface will act as ground plane for one frequency band, and will be transparent for two.

For satellite communications, several works have been done on dichroic sub-reflectors [9]–[19]. Most of these works offers two, three, and even four operation bands, where the dichroic surface acts as a band pass filter or a band stop filter. This allows working in the satellite with four frequency bands using one parabolic dish, thus reducing the number of parabolic dishes in the satellite.

Key contributions of this paper are as follows:

1) Design and optimize an IFSS, which works at three frequency bands, using intertwined structures. This warrants improved angular stability and is self-standing.
2) A mathematical interpretation, based on quasi-static analysis of the structure.
3) A physical interpretation, based on equivalent circuit model technique.
4) An understanding of the E- and H-Fields, which will help us to identify inductances and capacitances in the IFSS generated by an impinging plane wave.
5) A parametric study of the unit cell, which let us tune different frequency bands.
6) A description of PhotoChemical Machining process, which is used to manufacture the IFSS, and analyze the effects of rounded corners and beveled edges.

The main difference between our work, and previous works on dichroic surfaces for satellite antennas is the use a completely inductive frequency selective surface, which means that this structure does not need a substrate to have mechanical stability.

This paper is organized as follows: Section II comprises the unit cell design steps. It involves frequency requirements, unit cell design of both Brigid's and Jerusalem cross, and the combination of both shapes. In addition, reflection and transmission coefficients of TE mode are presented for single and double layer IFSS. Section III comprises equivalent circuit analysis of the designed FSS, as well as its mathematical background. In addition, the reflection coefficient obtained will be compared with the full wave simulation. Section IV comprises the parametric study of the IFSS. Section V comprises the experimental verification of our proposed IFSS. It involves the effects of the PCM manufacturing process, the measurement setup, and a comparison between simulated and measurement results.

TABLE 1. Proposed frequency bands for the IFSS operation as an application for satellite communications.

Band	Central Frequency	Required Bandwidth	Application
1	18.5 GHz	17.3-19.3 GHz	Fixed satellite service
2	24.6 GHz	24.5-25.5 GHz	ISM and Radio determination
3	30.1 GHz	29.1-31 GHz	Fixed satellite service

II. UNIT CELL DESIGN

First, to design a unit cell we need to know the frequency bands of operation and the required bandwidth. This information can be found in Table 1. The frequency bands presented are used in earth-to-satellite and satellite-to-earth communications in Europe [20], and were chosen as a proof of concept. Second, to fulfill the frequency operation and bandwidth requirements, resonant shapes were chosen. Some resonant shapes, and its frequency characteristics can be found in [1]. Once the resonant shapes had been chosen, the following characteristics must be obtained: dimensions, periodicity, metal thickness, lattice type and material. Those characteristics will dictate the resonant frequencies, bandwidth, onset of grating lobes, angular stability and polarization independence.

The resonant shapes chosen, which best suit our requirements, are: the intertwined Brigid's and Jerusalem cross apertures.

A. INTERTWINED BRIGID'S CROSS SHAPE

The intertwined Brigid's cross shape has been chosen due to its symmetry, and to its intertwined characteristics, which connects multiple adjacent unit cells. Both characteristics

leads to a more packed unit cell, improving angular stability and bandwidth. The fundamental mode resonates at arm lengths multiple of $\lambda_0/5$. This shape will generate the Band 1 requirements.

B. JERUSALEM CROSS SHAPE

The Jerusalem cross shape has good angular stability, isolated resonances, and can be highly packed [1]. Normally, this shape has two highly separated fundamental modes, the last is generally located at the grating lobe region and sometimes is mistakenly confused with a second harmonic. The first fundamental mode depends on the vertical aperture and horizontal aperture, in the case of a symmetric shape [1]. This etched shape will generate the frequency Band 3 requirements. Both, intertwined Brigid's and Jerusalem cross aperture shapes can be seen in Fig. 2.

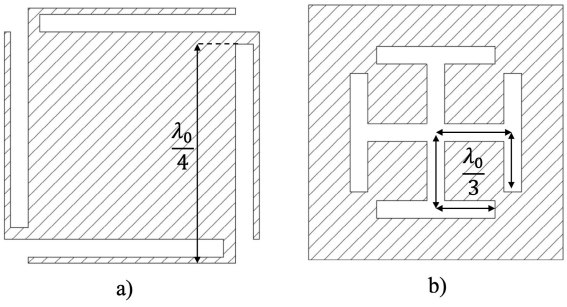

FIGURE 2. a) Intertwined Brigid's cross unit cell aperture with its approximate resonant frequency. b) Jerusalem cross unit cell aperture with its approximate resonant frequency. (Shaded region represents metal).

C. SINGLE LAYER INTERTWINED JERUSALEM CROSS IFSS

To acquire the final unit cell, and to generate the frequency Band 3, we intersect both unit cells etching the intertwined Brigid's cross in the Jerusalem cross aperture unit cell. The combination will generate a highly packed, multi-resonant and polarization independent unit cell. The resonant frequencies and bandwidth of this combined unit cell have a slight variations compared to separated shapes. This phenomenon can be explained due to coupling of the two etched shapes, generated by surface currents that are mainly placed in the apertures. These dimensions are a starting point to optimize the structure to resonate at the required frequencies and bandwidths. The structure was optimized using particle swarm optimization, embedded in CST Microwave Studio. The goals were: resonant frequencies, bandwidth, and polarization independency. The unit cell is presented in Fig. 3 and its dimensions are: $A = 1\ mm$, $B = 0.3\ mm$, $C = 0.15\ mm$, $D = 0.425\ mm$, $E = 0.2\ mm$, $F = 0.3\ mm$, $G = 0.2\ mm$, and $H = 0.3\ mm$. This structure has a thickness $T = 0.2\ mm$ and a lattice periodicity $P = 4.3\ mm$.

Transmission and reflection coeffcients were obtained using two Floquet ports separated $\frac{\lambda_0}{4}$ from the IFSS. The solver used was frequency domain and configured with

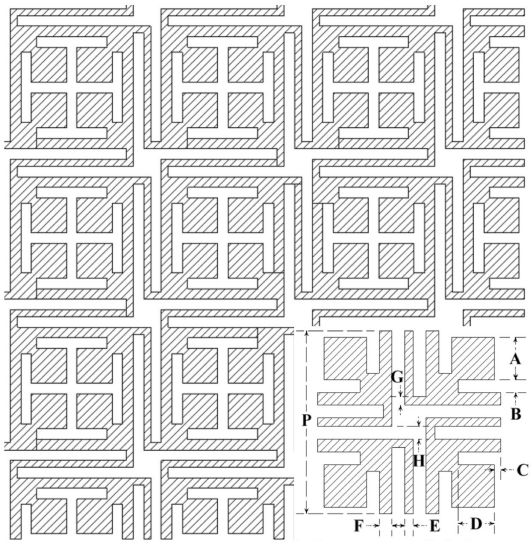

FIGURE 3. Unit cell dimensions, and full structure of an intertwined Jerusalem cross IFSS. (Shaded region represents metal).

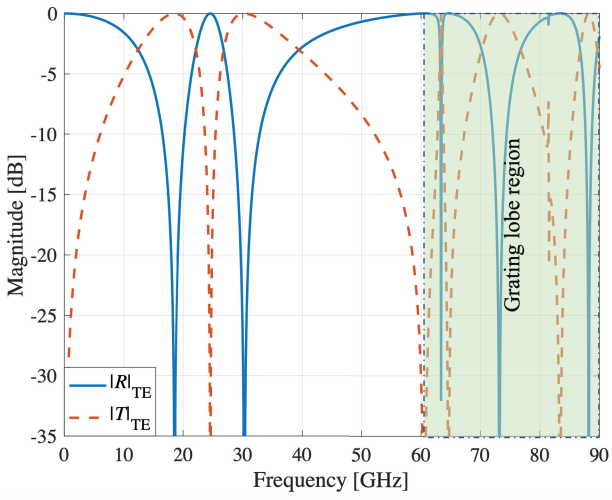

FIGURE 4. Simulated reflection and transmission coefficients of the IFSS presented in Fig. 3 at normal incidence of a vertically polarized wave.

a suitable mesh at the frequency range $0 - 90\ GHz$. This frequency range was selected to show the grating lobe region. TE mode was analyzed in reflection and transmission, as can be seen in Fig. 4. TM mode will not be analyzed due to symmetry of the IFSS. The IFSS has been analyzed using admittance Smith chart shown in Fig. 5, which helps us to characterize the IFSS operation at different frequency bands. At frequency Band 1 and 2, the IFSS is well matched to the free space admittance $Y_o \approx \frac{1}{377}$. Therefore, the structure will let thorough almost all the incoming electromagnetic waves. Conversely, at frequency Band 2, the admittance is poorly matched, acting as a ground plane reflecting all the incoming electromagnetic waves in the backscatter direction. It is worth to mention that the phase difference between reflected and incident electromagnetic wave is positive due to the inductive operation of the surface.

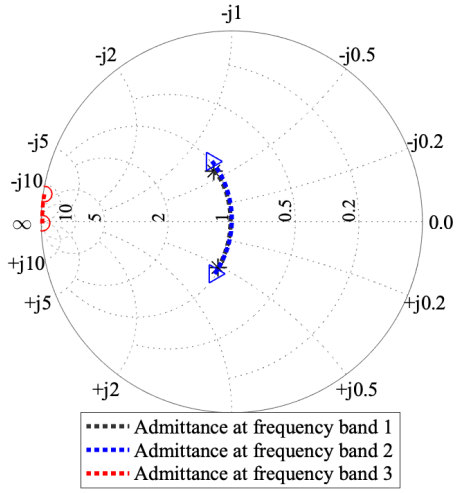

FIGURE 5. Smith chart representation of the IFSS simulated admittance presented in Fig. 3. The frequency bands presented are described in Table 1.

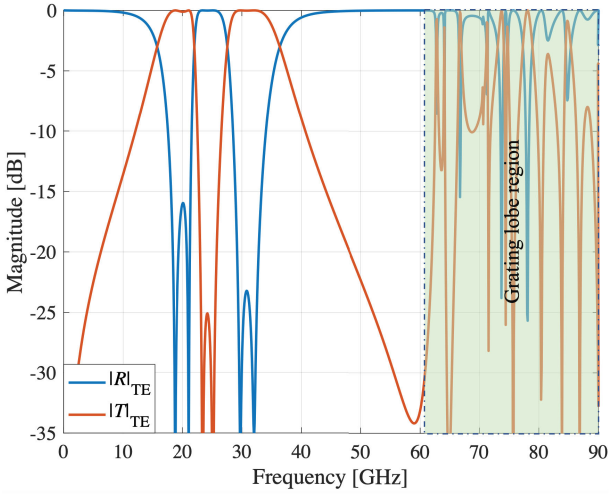

FIGURE 6. Simulated reflection and transmission coefficients of a double layer IFSS, presented in Fig. 3 at normal incidence of a vertically polarized wave.

D. DOUBLE LAYER INTERTWINED JERUSALEM CROSS IFSS

The roll-off, flatter top, and bandwidth can be improved by cascading two IFSS separated at a distance of less than $\lambda_0/4$ [1]. The distance was acquired through optimization at the frequency bands of interest. After the optimization process, the most suitable distance is 2 *mm*. Fig. 6 shows the simulation of a double layer IFSS.

III. EQUIVALENT CIRCUIT ANALYSIS OF THE IFSS

For simplicity, equivalent circuit for both shapes will be acquired separately, and finally, combined to obtain an equivalent circuit, which describes its multi-band operation.

1) JERUSALEM CROSS APERTURE

The work described in [3] is the first paper to our knowledge that proposes an equivalent circuit for a Jerusalem cross grid. A more detailed equivalent circuit that englobe both Jerusalem cross resonant frequencies was proposed in [21]. The equivalent circuit consists of two RLC series circuit connected in parallel. This leads us to think that the equivalent circuit for a Jerusalem cross aperture will be a two RLC parallel circuit connected in series. To verify this hypothesis, a full wave simulation was made, obtaining E- and H-Fields at the structure. After examining those fields, capacitors are represented by electric charge distribution in the apertures. Whereas, the metallic strips, where the magnetic field describes a curl, are represented by inductors [22].

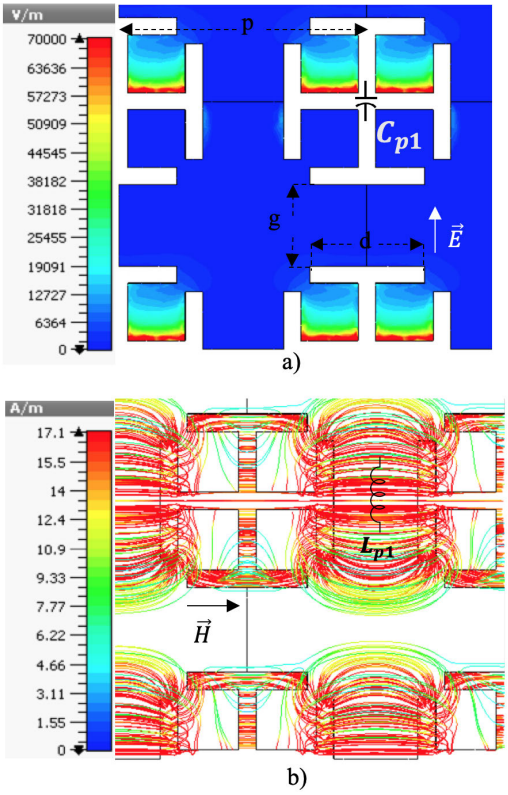

FIGURE 7. a) E-Field 2D contour of a vertically polarized wave, working at 29 *GHz*, b) H-Field lines of a vertically polarized wave, working at 29 *GHz*.

At the first resonant frequency, which is 29 *GHz*, the E-Field is strong in the horizontal middle aperture. This can be seen in Fig. 7a and can be represented using a capacitor. On the other hand, the strip that separates both Jerusalem cross shapes is surrounded by a curled H-Field. This can be seen in Fig. 7b and can be represented by an inductor with its embedded resistance. The connection between the capacitor and the inductor is parallel due to the inductive nature of the FSS. Neglecting the losses in the IFSS, it can be inferred through analysis that the equivalent circuit is $L_{p1}||C_{p1}$, because of the bandpass operation of the IFSS. It is worth to say that the second resonant frequency of the IFSS is placed at the grating lobe region. Therefore, it will not be considered. The equivalent circuit of the Jerusalem cross aperture can be seen in Fig. 11.

The impedance generated by each of the inductors and capacitor are:

$$Z_{Cp1} = \frac{-j}{\omega C_{p1}} \tag{1}$$

$$Z_{Lp1} = j\omega L_{p1} \tag{2}$$

respectively; therefore, the impedance of the circuit reads:

$$Z_T = j\omega_{z1}\frac{L_{p1}}{(1-\omega_{p1}^2 L_{p2} C_{p2})} \tag{3}$$

By Babinet's principle, the grid array is complementary to the aperture array [1]. Hence, the admittance expression for a Jerusalem cross grid array calculated in [7] is equal to the impedance calculated in our work. From (3), we can derive the values of the inductors and capacitors as follows. We can see that the impedance in (3) will be minimum at $\omega_{z1} = 0$, and maximum at a certain value of ω_{p1}. Clearly the value of ω_{p1} is our second resonance frequency. The value of the inductors and capacitors can be obtained through the following relation.

$$L_{p1} = \frac{1}{\omega_{p1}^2 C_{p1}} \tag{4}$$

The previous equation can be solved with the numerical value of C_{p1}. The work described in [21] proposes an equivalent-circuit-modeling technique, which allows to calculate an approximate value of reactance or susceptance of an FSS segment. By using this technique and (5)-(8), we will obtain an approximate value for C_{p1} susceptance, named B_{p1}. Then, to obtain the reflection and transmission coefficients we use (9) and (10) respectively. For a more accurate value, we used an iterative procedure that compares the IFSS reflection coefficient obtained through electromagnetic simulation with equivalent circuit simulation.

$$B_{p1} = \frac{4d\ \cos(\phi)}{\lambda} ln\ \csc(\frac{\pi g}{2p}) + G(p, g, \lambda, \phi) \tag{5}$$

where,

$$G(p, g, \lambda, \phi) = \frac{\frac{1}{2}(1-\beta^2)^2[((1-\frac{\beta^2}{4})(C_+ + C_-) + 4\beta^2 C_+ C_-)]}{1-\frac{\beta^2}{4} + \beta^2(1+\frac{\beta^2}{2}-\frac{\beta^4}{8})(C_+ + C_-) + 2\beta^6 C_+ C_-} \tag{6}$$

$$\beta = \sin(\frac{\pi w}{2p}) \tag{7}$$

$$C_\pm = \frac{1}{\sqrt{(\frac{p\sin\phi}{\lambda} \pm 1)^2 - (\frac{p}{\lambda})^2}} - 1 \tag{8}$$

$$|S_{11}| = \frac{Z_0}{2Z + Z_0} \tag{9}$$

$$|S_{12}| = \frac{2Z}{2Z + Z_0} \tag{10}$$

The values computed are: $C_{p1} = 167.14\ fF$ and $L_{p1} = 180\ pH$. Full wave simulations and equivalent circuit model simulations are shown in Fig. 8.

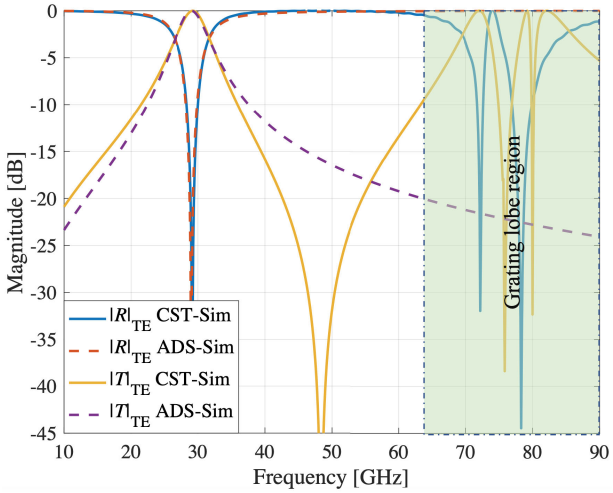

FIGURE 8. Full wave and circuit approach simulation of the Jerusalem cross aperture presented in Fig. 7 at normal incidence of a vertically polarized wave.

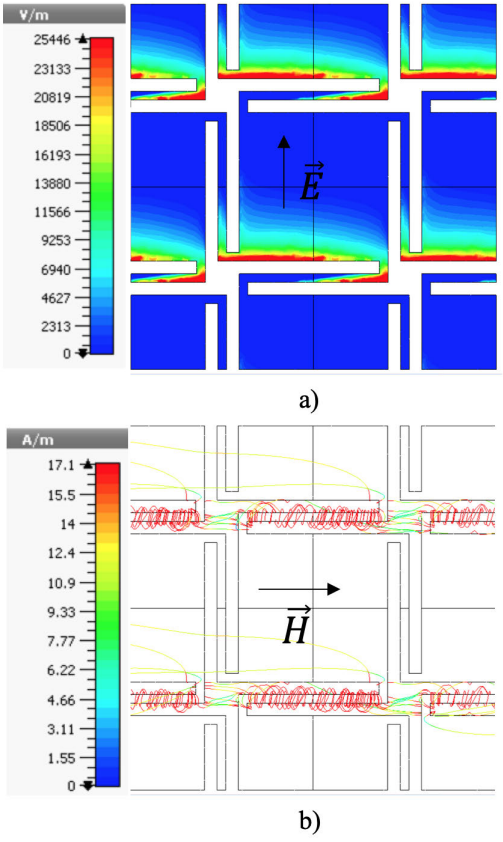

FIGURE 9. a) E-Field 2D contour of a vertically polarized wave, working at 18.5 *GHz*, b) H-Field lines of a vertically polarized wave, working at 18.5 *GHz*.

2) INTERTWINED BRIGID'S CROSS APERTURE

The intertwined Brigid's cross aperture can be analyzed using the same methodology as the Jerusalem cross. The E-Field and H-Field obtained through full wave simulation can be seen in Fig. 9a and Fig. 9b respectively. It can be inferred that the intertwined Brigid's cross aperture can be represented

using a parallel LC circuit, as shown in Fig. 11. The structure equivalent impedance is presented in (11).

$$Z_T = j\omega_{z3}\frac{L_{p3}}{1-\omega_{p3}^2 L_{p3}C_{p3}} \tag{11}$$

Using (11) we can see that the IFSS will have a minimum at $\omega_{z3} = 0$ and a maximum at ω_{p3}, which in this case is our second resonance frequency. After applying the previous formulas, we obtain, $L_{p3} = 1.27\ nH$ and $C_{p3} = 55\ fF$. Full wave simulation and equivalent circuit model simulation can be seen in Fig. 10.

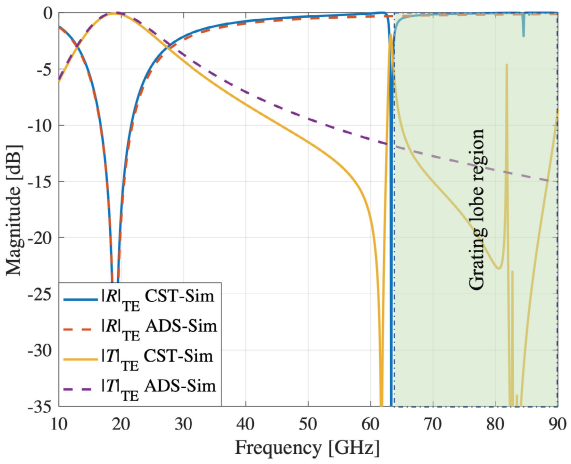

FIGURE 10. Full wave and circuit approach simulation of the intertwined Brigid's cross aperture, presented in Fig. 11 at normal incidence of a vertically polarized wave.

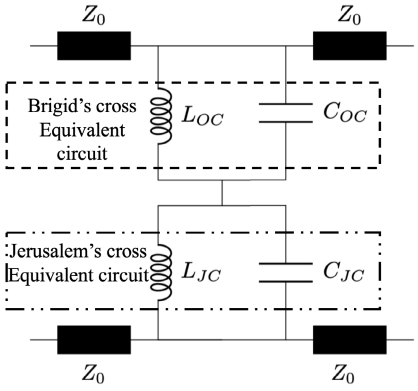

FIGURE 11. Equivalent circuit of an intertwined Jerusalem cross aperture, where $L_{OC}||C_{OC}$ represents the first band pass generated by the Brigid's cross aperture, $L_{JC}||C_{JC}$ represents the second resonant frequency generated by the Jerusalem cross aperture, and Z_o represents the free space impedance. $L_{OC} = 0.962\ nH$, $C_{OC} = 76\ fF$, $L_{JC} = 0.4313\ nH$, $C_{JC} = 64.3\ fF$.

The final equivalent circuit, which is shown in Fig. 11, represents the intertwined Jerusalem cross IFSS. This circuit consists on a series connection of branches $L_{p1}||C_{p1}$, which corresponds to the first resonance frequency of the Jerusalem cross, with $L_{p3}||C_{p3}$, which corresponds to the Brigid's cross resonance frequency. This connection is possible because of the band-pass nature of this structure. Equivalent circuit is represented in the physical structure by drilling the Jerusalem cross structure into the Brigid's cross, as shown in Fig. 3. The previously calculated capacitances and inductances are affected by this combination, and new values were obtained using the same curve fitting method. Basically, the previously calculated inductance L_{p1} is lower than the new inductance L_{JC} due to the magnetic field circulating in the plate between Jerusalem cross apertures. This increases as the effective metallic area is reduced. The previously calculated C_{p1} value is greater than the new C_{JC} capacitance due to the mutual coupling of both structures, which reduces the electric field in the center of the cross. The values of L_{p3} and C_{p3}, which now are called L_{OC} and C_{OC}, suffer variations but to a lesser extent, since both values depend exclusively on the interweaving generated in both arms of the Brigid's cross. The final unit cell was simulated in CST and ADS respectively, and shown in Fig. 12.

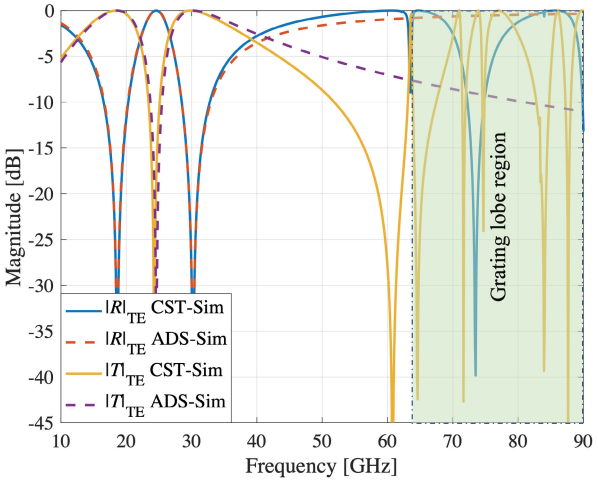

FIGURE 12. Full wave and circuit approach simulation of the Jerusalem cross aperture and intertwined Brigid's cross aperture, at normal incidence of a vertically polarized wave.

IV. PARAMETRIC STUDY OF THE PROPOSED IFSS

A parametric study was performed to understand the effects of variation in frequency and bandwidth due to the change in length and width of the unit cell apertures. To keep the period constant, variations of the apertures will be compensated with variations in metal length. As the unit cell is symmetric, only TE mode reflection coefficient will be shown.

1) Parameter G (Metal strip between Brigid's crosses)
Since G variation only affects the size of the displaced cross arms and not to the period of the unit cell; therefore, no other parameter will be modified to compensate this variation. Fig. 13 shows by increasing G, from 0.1 mm to 0.4 mm, increases the first resonance frequency. Increasing this parameter, the electrical length of the Brigid's cross aperture is reduced; therefore, the first resonance frequency is increased. It should be

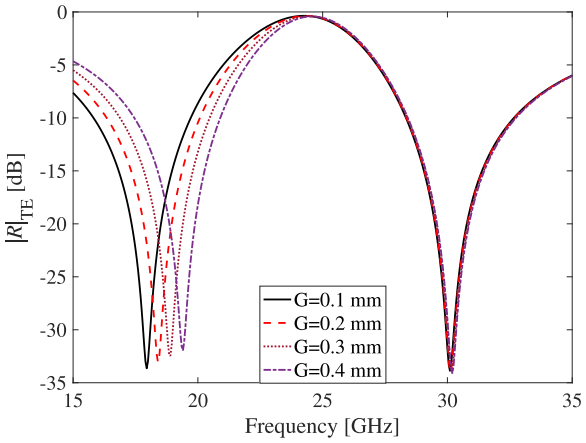

FIGURE 13. Reflection coefficient of the proposed unit cell when *G* varies. The original value of *G* is 0.2 *mm*.

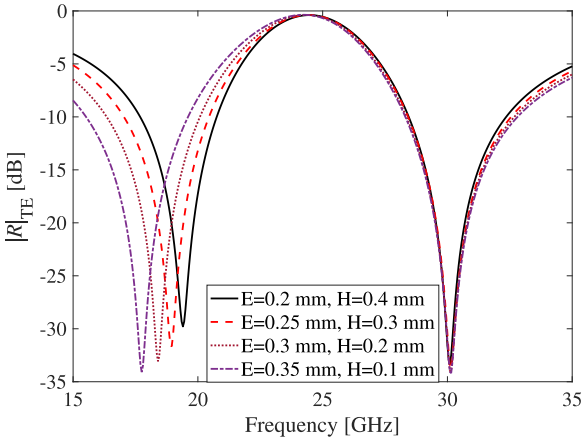

FIGURE 14. Reflection coefficient of the proposed unit cell when the variated parameter are *D* and *C*. Original value of *H* is 0.3 *mm* and *E* is 0.2 *mm*.

noticed that tuning of this first resonance frequency is totally independent of the second resonant frequency, but affects the total reflection band, which is reduced as G increases.

2) Parameter H (Brigid's cross arms width)
When increasing H the value of E is reduced to keep the same period. Increasing H and reducing E, the associated capacitance is reduced while the associated inductance increases; therefore, the quality factor Q is reduced, thus increasing the bandwidth of the first resonance frequency. This effect can be seen in Fig. 14. It is worth mentioning that these variations do not affect the second resonance frequency, but they do affect the total reflection band, increasing it as H increases.

3) Parameter D (Jerusalem cross loading arm length)
By increasing the loading length of the Jerusalem cross, the inductance generated by the metal plate separating the two crosses increases; therefore, and using equation (4), the second resonance frequency is reduced, as shown in Fig. 15. It should be mentioned that these variations do not affect the first resonance frequency, but affect the total reflection band, increasing it.

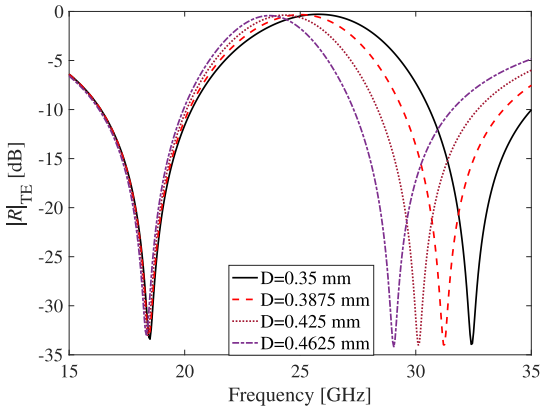

FIGURE 15. Reflection coefficient of the proposed unit cell when the variated parameter is *H*. The original value of *H* is 0.85 *mm*.

4) Parameter B (Jerusalem cross loading arm width)
By varying the loading aperture B of the Jerusalem cross we can control both the second resonance frequency and the reflection band. When increasing B, F is reduced to keep the same period. This variation entails that the metallic strip placed above the loading arm gets thinner, increasing the inductance associated; therefore, the Q factor is reduced; thus, increasing bandwidth. On the other hand, as the aperture gets thicker the capacitance associated gets bigger, decreasing the resonant frequency. Fig. 16 show that as B gets bigger, the second resonance frequency is reduced, and the bandwidth increases. Finally, as we mention earlier; as B increases the reflective frequency band, and the bandwidth decreases.

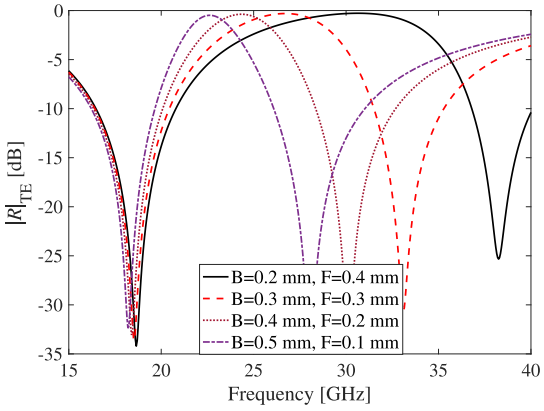

FIGURE 16. Reflection coefficient of the proposed unit cell when the variated parameter are *B* and *F*. The original value of *B* is 0.3 *mm* and *F* 0.3 *mm*.

V. EXPERIMENTAL VERIFICATION

The proposed concept of an IFSS using intertwined shapes has been validated through experimentation. The material used for the manufacturing was stainless steel 304 with thickness of 0.2 *mm* and $\sigma = 720\ n\Omega$. Even though this material

has less conductivity than copper, it has high strength, and corrosion resistance. If we want to improve the conductivity, we could consider to metallize the structure with cooper. Two prototypes were designed using 36-unit cells with an overall dimension of 200 × 200 *mm*. Near the sided edges of the structure 8 holes were placed to hold a frame for measuring purposes.

A. IFSS MANUFACTURING PROCESS

Before choosing a manufacturing method, we need to consider some design parameters, such as: smallest aperture size, which is ≈200 μm, hardness, and thickness of the material. After a research of the available manufacturing techniques, the better that suits our purposes is Photochemical Machining (PCM).

1) PHOTOCHEMICAL MACHINING

This method follows the same principle as PCB manufacturing. It has an accuracy of 13 μm and the sheet thickness varies from 0.013 to 2.032 *mm*. It has a major limitation represented by non-uniform etching through apertures. That is, the etchant will not attack the metal perpendicularly to the resistive sheet; instead, it will attack sidewalls and under the resistive film. Depending on the manufacturer, there are a variety of etching techniques, which offers different bevel finishing at the edges. The most common PCM techniques are: one and two-sided etching. On One-sided etching, the resistive stencil is placed over the upper face of the metal sheet and a complete resistive sheet over the other face, as illustrated in Fig. 17b. The bevel in one-sided etching is approximate $d = 0.4\ t$, being t the thickness of the metal sheet. In Two-sided etching, the resistive stencils are placed over both faces of the metal sheet, as illustrated in Fig. 17a. The bevel in two-sided etching is approximate $D = 0.2\ t$ to $D = 0.1\ t$ and the bevel is uniform in both faces. Both etching techniques have an under etching in the resistive film that is approximate to $g = 0.02\ t$.

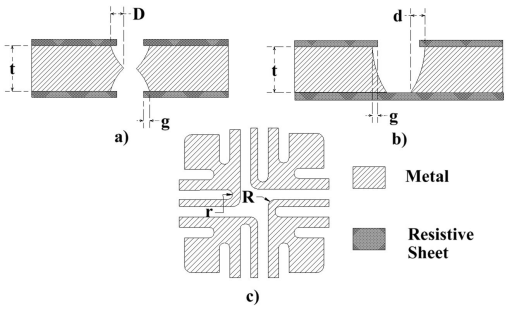

FIGURE 17. a) Cross sectional view of a prototyped metal sheet using two-sided PCM. b) Cross sectional view of a prototyped metal sheet using one-sided PCM. c) Front view of the unit cell after etching using PCM.

In addition, rounded corners are created in both etching techniques. Depending on the corner, the radius could be external R or internal r, as illustrated in Fig. 17c.

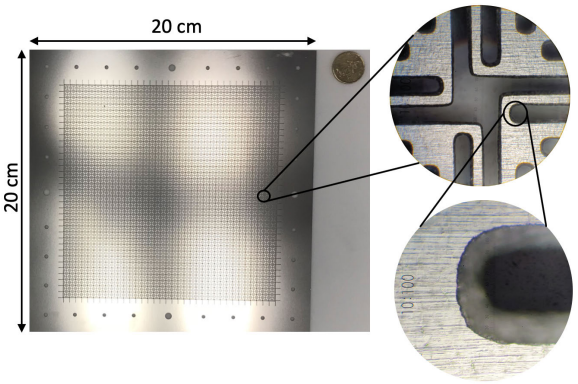

FIGURE 18. IFSS prototyped using a 0.2 *mm* thick sheet of stainless steel 304 and a zoomed view of a unit cell.

External radius is approximate $R = 0.4\ t$ to $R = 0.6\ t$ and internal radius is $r = 0.8\ d$ to $r = d$ [23].

B. EFFECTS IN ROUNDED CORNERS AND BEVELED EDGES

The manufacturer offered both one-sided and two-sided etching. To understand the effects of either, and to choose one that better suits our research purposes, the original unit cell was modified to simulate both etching methods. Recommendations of the manufacturer for both etching methods are: inner radius $r = t$, outer radius $R = 0.5t$, bevel for one-sided etching $d = 0.4t$ and for two-sided etching $D = 0.2t$. Stainless steel 304 was selected as material for the IFSS unit cell. S-Parameters comparison between those two etching methods and the original unit cell design are shown in Fig. 19.

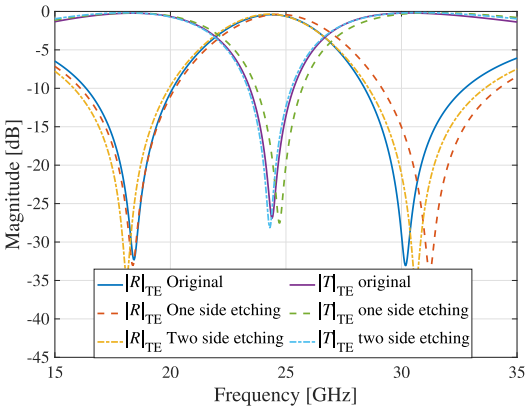

FIGURE 19. Reflection and transmission coefficients simulation of an original designed IFSS, one-sided etching and two-sided etching method. Both methods use an inner radii $r = t$ and outer radii $R = 0.5t$.

In the first resonance frequency the S-Parameters for the original and one-sided etching are nearly the same, with a light increase in bandwidth of the latter. On the other hand, two-sided etching has a resonance frequency shift of 0.3 *GHz*. In the second resonance frequency, the S-Parameters have a more marked difference. The resonance frequency is shifted upward 0.4 *GHz* for two-sided etching and 1.3 *GHz* for one-sided etching with respect to the original design. This variation can be explained due to the reduction on the

Jerusalem cross arm length and width due to the etching process. This shift is bigger in one-sided etching because the bevel edge is bigger. The transmission coefficient shows a bigger shift upward in one-sided etching than two-sided due to the same reasons previously explained. As a result, we choose two-sided etching to avoid unwanted frequency displacement and to keep cardinal symmetry.

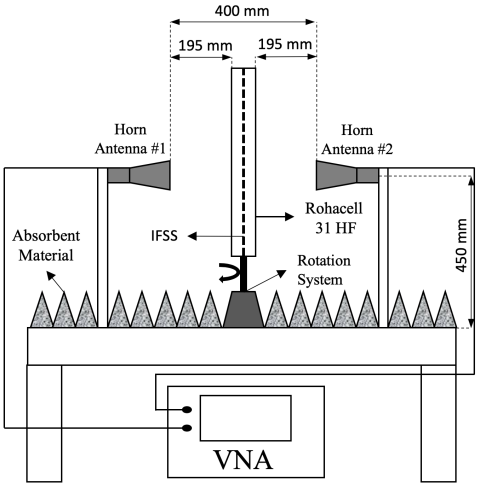

FIGURE 20. Schematic illustration of the measurement setup, which includes distance form antennas and from SUT.

C. MEASUREMENT SETUP

The manufactured IFSS has been characterized by measuring transmission and reflection coefficients using an optical bed configuration. The measurement setup shown in Fig. 20 was configured as follows: Two double ridged horn antennas model DRH40 were placed away form each other a distance of 400 *mm* and 450 *mm* above a rail using a support system. Although both antennas were placed at a distance that warranties correct illumination, they are placed in the near-field region to avoid using lents. At the middle, a motorized rotation stage (MRS), model MOR-100-30 was placed over a rail. This rotates the Surface Under Test (SUT) to a different angles of incidence. The SUT was fastened using a 1 *cm* thick frame made of a ROHACELL 31HF which has an $\epsilon_r = 1.041$. This frame was placed in the MRS fastening system. A photo of the measurement setup can be seen in Fig. 21. Both antennas outputs are connected through coaxial cable to a Vector Network Analyzer (VNA) Rohde&Schwarz ZVA 67. Surrounding the measurement setup absorbent material was placed to reduce unwanted reflections. The VNA frequency range was configured from 5 to 35 *GHz* with a step size of 50 *MHz*. The number of points was set to 1024 with a frequency span of 13 *GHz*. To enhance measurements results, time gating was applied to the RAW data. This reduces deceptive backscattering caused by multi-path propagation. For reflection measurements, two stages were configured. Normal incident measurements were performed using one antenna. For angles above 0 *degrees* measurements were made using two antennas. The latter case, both antennas will be separated by an angle centered in the middle of the IFSS.

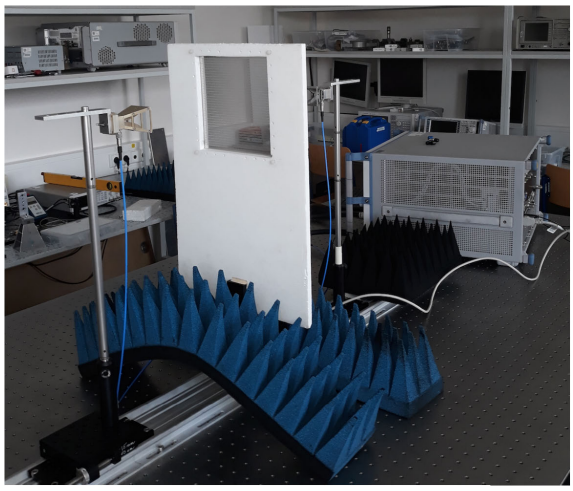

FIGURE 21. Photo of the measurement setup which includes both double ridged horn antennas model DRH40, rail, motorized rotation stage, SUT, and a VNA.

D. SINGLE LAYER IFSS

The prototype was characterized using the configuration previously described. The S-Parameters measurements obtained to normal incidence illumination for both modes show accordance with simulations, with a slight variation in bandwidth and frequency displacement at the first resonance frequency, as can be seen in Fig. 22 for TE mode, and Fig. 23 for TM mode. This variation in bandwidth is most likely due to: measurement mismatches, one antenna measurement technique and manufacturing tolerances.

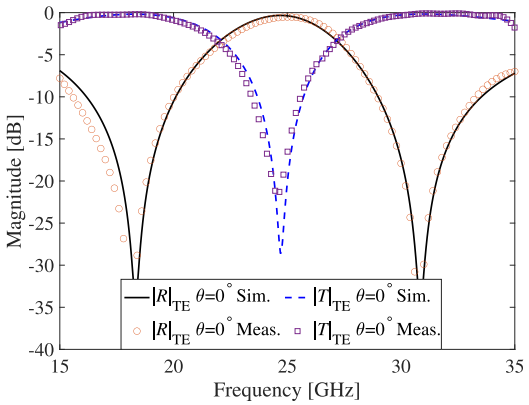

FIGURE 22. TE mode measured and simulated reflection and transmission coefficient at normal incidence for a single layer IFSS.

In TE mode and for non-normal incidence angles, variations between measured and simulated results are seen in both reflection and transmission coefficients. For the reflection coefficient, which is shown in Fig. 24, the first resonance frequency position and bandwidth are in better accordance with simulation, compared to the normal incidence results. Once more, this is due to the two antenna measurement

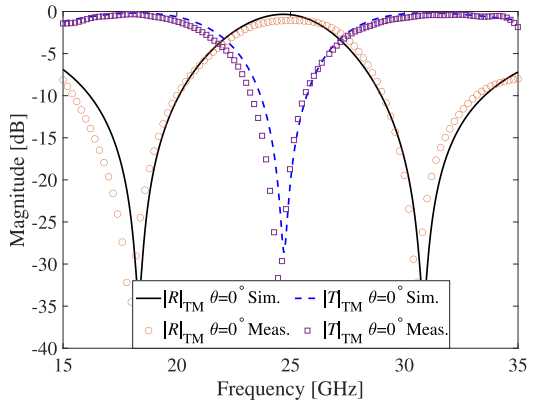

FIGURE 23. TM mode measured and simulated reflection and transmission coefficient at normal angle of incidence for a single layer IFSS.

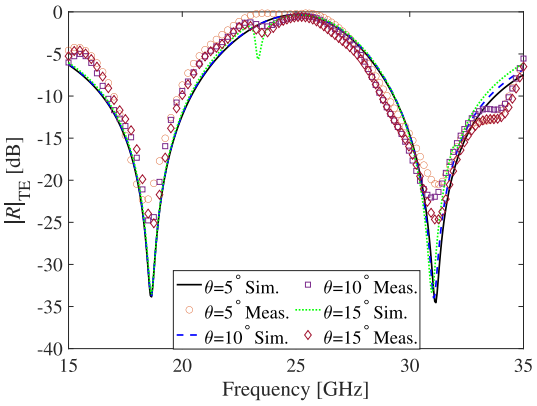

FIGURE 24. TE mode measured and simulated reflection coefficient of a single layer IFSS at oblique incidence.

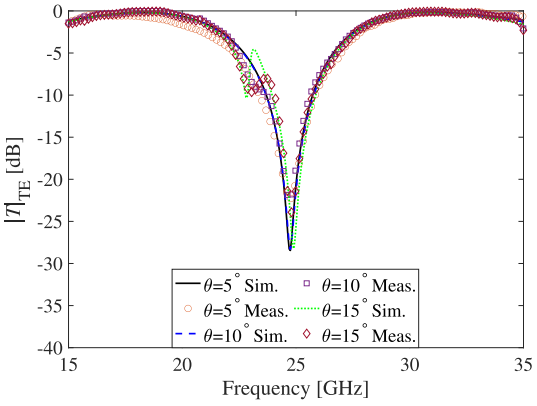

FIGURE 25. TE mode measured and simulated transmission coefficient of a single layer IFSS at oblique incidence.

technique, which is more accurate. In addition, the measured reflection coefficients show a slight variation in bandwidth at the first resonance frequency, and a more pronounced variation at the second resonance frequency, compared to normal incidence case results because angular stability decreases for resonances above the first. On the other hand, for transmission measurements, which are shown in Fig. 25, have two nulls instead of one as for the case of normal incidence. This new null appears at 22 *GHz* and is present only for TE mode at oblique angles of incidence, in this case angles above 10 *degrees*. This null is generated by the so called bend or crooked mode, which can be explained using a modal analysis, depicted in [1].

For TM mode measured and simulation results, shown in Fig. 26 and Fig. 27, are almost the same as for TE mode with the difference that the crooked mode is not present anymore, and the angular stability has been improved. This is because the surface rotation axis is not the same as the electric field orientation.

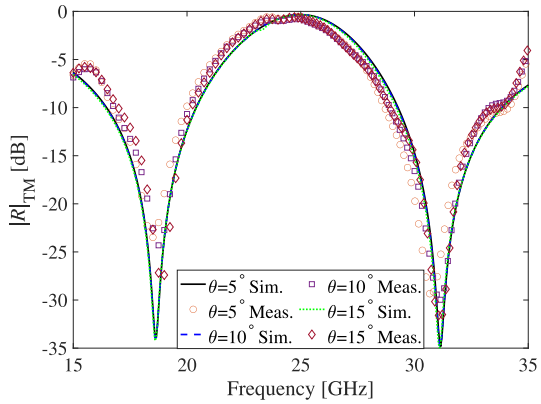

FIGURE 26. TM mode measured and simulated reflection coefficient of a single layer IFSS at oblique incidence.

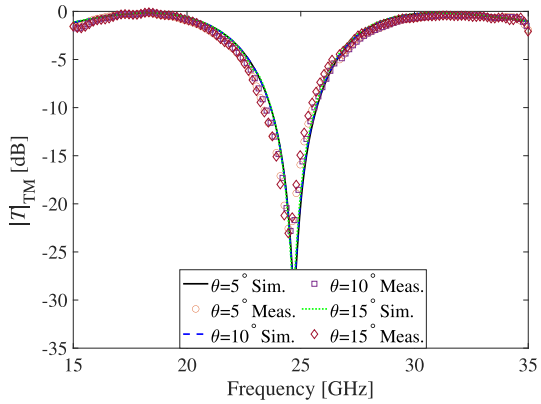

FIGURE 27. TM mode measured and simulated transmission coefficient of a single layer IFSS at oblique incidence.

E. DOUBLE LAYER IFSS

As can be seen in the results for single layer IFSS, the resonance frequencies and bandwidth are nearly at the limit compared with the design requirements, shown in Table 1. To improve the results we need to increase bandwidth, flatter the top, and faster roll-off. This can be done by placing two IFSS in cascade, separated by a distance of 2 *mm* from each other. To have mechanical stability for measurement purposes, a sheet of 2 *mm* ROHACELL 31HF was placed between both IFSS. Measured and simulated reflection and transmission coefficients at different angles of incidence for TE mode are shown in Fig. 28 and Fig. 29 respectively, and for TM mode in Fig. 30 and Fig. 31.

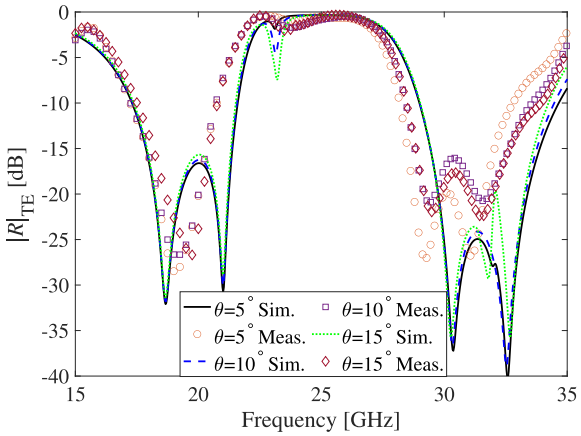

FIGURE 28. TE mode measured and simulated reflection coefficient of a double layer IFSS at oblique incidence.

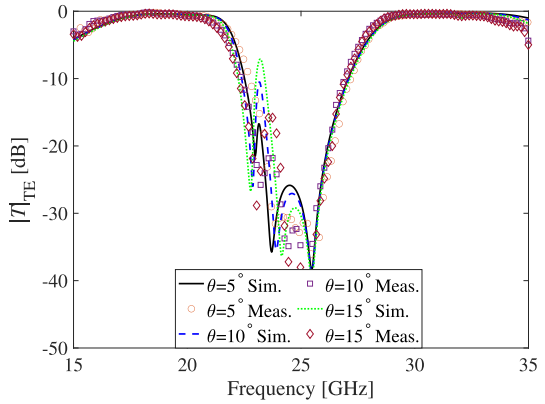

FIGURE 29. TE mode measured and simulated transmission coefficient of a double layer IFSS at oblique incidence.

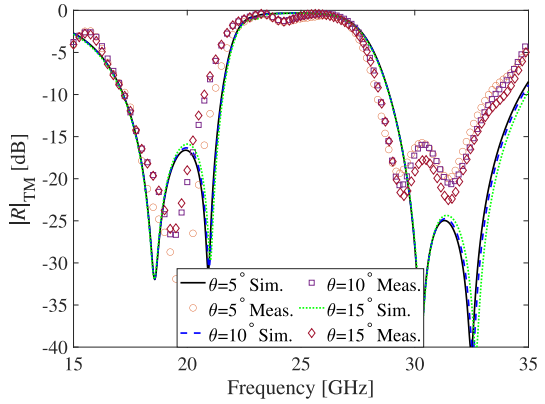

FIGURE 30. TM mode measured and simulated reflection coefficient of a double layer IFSS at oblique incidence.

As is expected, for both modes the results show an increase in bandwidth, flatter top, and faster roll-off compared with single layer configuration. Some differences can be observed between simulated and measured results. First, for both TE and TM mode reflection coefficients, which are shown in Fig. 28 and Fig. 30, the first resonance frequency measured bandwidth is slightly smaller than the simulated. This can be explained by the mismatch alignment of both FSS. Second, both reflection coefficient are shifted slightly to

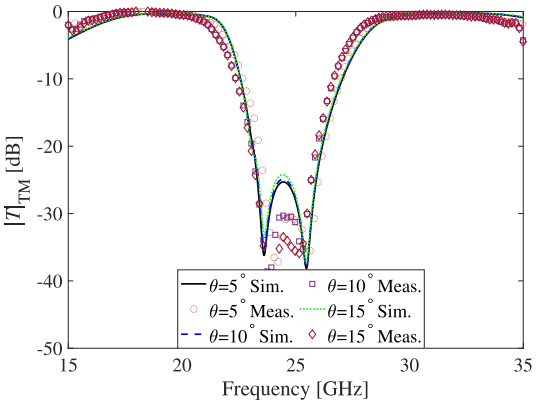

FIGURE 31. TM mode measured and simulated transmission coefficient of a double layer IFSS at oblique incidence.

the left. This is due to the addition of the foam that generates a frequency shift. On the other hand, there are some slight variations between the measured results between different angles of incidence. The bandwidth and reflection variation are still present due to the same reasons explained before in single layer measurements. The crooked mode is still present at 23 *GHz*, for TE mode. In TM mode the crooked mode is not present and the angular stability has been improved. Using this cascade configuration we can see that the IFSS works fine over the frequency bands of interest.

VI. CONCLUSION

An intertwined inductive FSS has been designed and manufactured working as a dichroic sub-reflector for Ku, K, and Ka bands. It has been successfully demonstrated that an IFSS using intertwined shapes can be used to work as a multi-band dichroic sub-reflector. E- and H-Fields on the structure were analyzed to understand their filter capabilities, and to visualize the generated inductances and capacitances when a plane wave impinges on the surface. Additionally, an equivalent circuit model for the IFSS has been proposed, allowing us to understand the effects of increasing or decreasing the size of apertures or strips. A parametric study of the unit cell was performed, showing the independence tuning for both resonant frequencies and bandwidth control. The effects of Photochemical Machining manufacturing process, such as rounded corners and edge bevels has been analyzed and compared with the original IFSS determining its effects. Two-sided etching method was selected due to the symmetrical operation of the IFSS and less impact in frequency and bandwidth shift. Finally, a dual layer configuration was designed and manufactured improving flatter top and faster roll-off. Simulations and measurements for both, single and double layer IFSS show good agreement and good angular stability for this application, specially in TM modes.

REFERENCES

[1] B. A. Munk, *Frequency Selective Surfaces: Theory and Design*. Hoboken, NJ, USA: Wiley, 2000, pp. 35–37.

[2] J. M. Rigelsford, S. M. Benito, and A. Vallecchi, "A tri-band inductive frequency selective surface sub-reflector for satellite communications systems," in *Proc. 8th Eur. Conf. Antennas Propag. (EuCAP)*, The Hague, The Netherlands, Apr. 2014, pp. 898–900.

[3] I. Anderson, "On the theory of self-resonant grids," *Bell System Tech. J.*, vol. 54, no. 10, pp. 1725–1731, Dec. 1975.
[4] M. Ohira, H. D. Eguchi, M. Tsuji, and H. Shigesawa, "Analysis of frequency selective surface with arbitrarily shaped element by equivalent circuit model," *Electron. Commun. Jpn. (Part II, Electron.)*, vol. 88, no. 6, pp. 9–17, Jun. 2005.
[5] A. L. P. S. Campos, A. Martins, and V. A. Almeida Filho, "Synthesis of frequency selective surfaces using genetic algorithm combined with the equivalent circuit method," *Microw. Opt. Technol. Lett.*, vol. 54, no. 8, pp. 1893–1897, Aug. 2012.
[6] M. W. B. Silva and L. C. Kretly, "An efficient method based on equivalent-circuit modeling for analysis of frequency selective surfaces," in *SBMO/IEEE IEEE MTT-S Int. Microw. Symp. Dig. Optoelectron. Conf. (IMOC)*, Rio de Janeiro, Brazil, Aug. 2013, pp. 1–4.
[7] F. Costa, A. Monorchio, and G. Manara, "An overview of equivalent circuit modeling techniques of frequency selective surfaces and metasurfaces," *Appl. Comput. Electromagn. Soc. J.*, vol. 29, no. 12, pp. 960–976, Dec. 2014.
[8] K. Chang, *Frequency Selective Surfaces-Encyclopedia of RF and Microwave Engineering*. Hoboken, NJ, USA: Wiley, 2005, pp. 1701–1706.
[9] M. Floreani, R. Zich, and G. Aulisio, "Design and experimental validations of a new shaped subreflector geometry for EMC oriented Cassegrain system," in *Proc. Asia-Pacific Conf. Environ. Electromagn. (CEEM)*, Nov. 2002, pp. 167–169.
[10] A. Vallecchi, J. M. Rigelsford, and S. Martin Benito, "An inductive dichroic surface for reflector antennas," in *Proc. IEEE Antennas Propag. Soc. Int. Symp. (APSURSI)*, Memphis, TN, USA, Jul. 2014, pp. 2070–2071.
[11] A. Vallecchi and A. G. Schuchinsky, "Analytical model of interwoven spiral arrays," *IET Microw., Antennas Propag.*, vol. 8, no. 15, pp. 1268–1276, Dec. 2014.
[12] S. S. Roy, T. N. Sekhar, C. S. Padmavathy, K. Bhattachariya, M. N. Kumar, and C. Saha, "Design of double layers dichroic subreflector for S and X band Cassegrain antenna," in *Proc. IEEE Indian Antenna Week (IAW)*, Madurai, India, Jun. 2016, pp. 47–50.
[13] P. Ingvarson, F. Johansson, and L. Pettersson, "A dichroic subreflector for a communication satellite," in *Dig. Antennas Propag. Soc. Int. Symp.*, San Jose, CA, USA, vol. 2, Jun. 1989, pp. 1088–1091.
[14] D. Bresciani, S. Contu, C. Bruno, and G. Crone, "Design of a 1 m dichroic subreflector for K_u/K_a frequency bands," in *Dig. Antennas Propag. Soc. Int. Symp.*, San Jose, CA, USA, vol. 2, Jun. 1989, pp. 1084–1087.
[15] C. Bruno, S. Contu, D. Marzi, and G. Mascolo, "Design, manufacturing and testing of a Ku/Ka dichroic subreflector for space communications," in *Proc. 8th Int. Conf. Antennas Propag.*, vol. 1, Mar./Apr. 1993, pp. 178–181.
[16] T. Mok, A. Allam, J. Vardaxoglou, and E. Parker, "Curved and plane frequency selective surfaces: A study of two offset subreflectors," *J. Inst. Electron. Radio Eng.*, vol. 58, no. 6, p. 284, 1988.
[17] M. Han, M. He, H. J. Sun, G. Q. Zhao, and H. Cheng, "Analysis of Cassegrain antenna by using a dichroic sub-reflector," in *Proc. IEEE Int. Conf. Microw. Technol. Comput. Electromagn.*, vol. 1, Aug. 2013, pp. 58–60.
[18] T. Wu, "Double-square-loop FSS for multiplexing four (S/X/Ku/Ka) bands," in *Antennas Propag. Soc. Symp. Dig.*, London, ON, Canada, vol. 3, Jun. 1991, pp. 1885–1888.
[19] R. Orr, V. Fusco, D. Zelenchuk, G. Goussetis, E. Saenz, M. Simeoni, and L. Salghetti Drioli, "Circular polarization frequency selective surface operating in Ku and Ka Band," *IEEE Trans. Antennas Propag.*, vol. 63, no. 11, pp. 5194–5197, Nov. 2015.
[20] Electronic Communications Committee, "The European table of frequency allocations and applications in the frequency range 8.3 Khz to 3000 Ghz (ECA table)," in *Proc. Eur. Conf. Postal Telecommun. Admin. (CEPT)*, 2013, pp. 1–262.
[21] C. Lee and R. Langley, "Equivalent-circuit models for frequency-selective surfaces at oblique angles of incidence," *IEE Proc. H-Microw. Antennas Propag.*, vol. 132, no. 6, p. 395, 1985.
[22] W. Li, C. Wang, Y. Zhang, and Y. Li, "A miniaturized frequency selective surface based on square loop aperture element," *Int. J. Antennas Propag.*, vol. 2014, pp. 1–6, 2014, Art. no. 701279.
[23] D. Allen, "Photochemical machining: From 'manufacturing's best kept secret'to a $6 billion per annum, rapid manufacturing process," *CIRP Ann.*, vol. 53, no. 2, pp. 559–572, 2004.

JUAN A. VÁSQUEZ-PERALVO was born in Quito, Ecuador. He received the B.Eng. degree in electronics and telecommunications from the Escuela Politêcnica Nacional, Quito, Ecuador, in 2012, the M.Sc. degree in wireless communication systems from The University of Sheffield, U.K., in 2015. He is currently pursuing the Ph.D. degree with Universidad Politécnica de Madrid. His current research interests are antenna design, frequency selective surfaces, and artificial magnetic conductors.

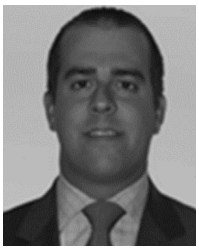

JOSÉ-MANUEL FERNÁNDEZ-GONZÁLEZ (Senior Member, IEEE) was born in Lausanne, Switzerland. He received the Diplôme dIngénieur en Électricité degree from the École Polytechnique Fédérale de Lausanne, Lausanne, in 2003, and the Ph.D. degree from the Universidad Politécnica de Madrid, Madrid, Spain, in 2009. In 2006, he joined the Centre de Recherches Poly-Grames, l'École Polytechnique de Montréal, Montreal, QC, Canada, and he joined the Chalmers University of Technology, Göteborg, Sweden, in 2007, as a Guest Ph.D. Student. From 2013 to 2019, he was an Assistant Professor with the Universidad Politécnica de Madrid. In 2018, he was a Fulbright Visiting Researcher with the Antenna Research Group, University of Colorado at Boulder. Since 2019, he has been an Associate Professor with the Universidad Politécnica de Madrid. He has authored more than 90 publications in scientific journals, symposium proceedings and seminars, and he holds four patents. He has participated in more than 35 research projects and contracts. His current research interests include phased array antennas, RF circuits, and metamaterial structures with emphasis on planar antenna applications.

PAVEL VALTR received the Ing. (M.Sc.) and Ph.D. degrees in radio electronics from Czech Technical University in Prague, Prague, Czech Republic, in 2004 and 2007, respectively. From 2007 to 2009, he was a Research Fellow with the University of Vigo, Vigo, Spain, working on various topics in electromagnetic wave propagation, including rough surface and vegetation scattering and land mobile satellite channel modeling. In 2009, he joined the European Space Agency (ESA/ESTEC), Noordwijk, The Netherlands, as a Postdoctoral Research Fellow. Since 2012, he has been with Czech Technical University in Prague, as a Researcher. His research interests include radiowave propagation for terrestrial and satellite applications, frequency selective surfaces, and computational methods in electromagnetics. Dr. Valtr was a recipient of the Young Scientist Award of XXVIII General Assembly from the International Union of Radio Science (URSI), in 2005.

JONATHAN M. RIGELSFORD (Senior Member, IEEE) received the M.Eng. and Ph.D. degrees in electronic engineering from the University of Hull, Hull, U.K., in 1997 and 2001, respectively. From 2000 to 2002, he was a Senior Design Engineer with Jaybeam Limited. From 2002 to 2014, he was a Senior Experimental Officer of the Communications Group, Department of Electronic and Electrical Engineering, The University of Sheffield, Sheffield, U.K., where he became a Senior Research Fellow, researching in the areas of RF propagation, biomedical electromagnetics, adaptive antennas, RFID, and cyber security. In February 2019, he moved back into industry to become RF Engineering Lead at Sensata Technologies.